Statistical analyzing the effect of ionospheric irregularity on GNSS radio occultation atmospheric measurement

Mingzhe Li [1,2,3,4], Xinan Yue [1,2,3,4]

[1] Key Laboratory of Earth and Planetary Physics, Institute of Geology and Geophysics, Chinese Academy of Sciences, Beijing, China

[2] Innovation Academy for Earth Science, CAS, Beijing, China

[3] Beijing National Observatory of Space Environment, Institute of Geology and Geophysics, Chinese Academy of Sciences, Beijing, China

[4] College of Earth and Planetary Sciences, University of Chinese Academy of Sciences, Beijing, China

Correspondence to: Xinan Yue (yuexinan@mail.iggcas.ac.cn)

Abstract. The Global Navigation Satellite System (GNSS) atmospheric radio occultation (RO) has been an effective method for Earth's atmosphere exploring. RO signals propagate through ionosphere before reaching the neutral atmosphere. The GNSS signal is affected by the ionospheric irregularity including the sporadic E (Es) and the F region irregularity due to mainly multipath effect. The effect of ionospheric irregularity on atmospheric RO data has been demonstrated by several studies in terms of cases. However, its statistical effect has not been investigated comprehensively. In this study, based on the Constellation Observing System for Meteorology, Ionosphere, and Climate (COSMIC) RO data during 2011-2013, the failed inverted RO events occurrence rate and the bending angle oscillation, which is defined as the standard deviation of the bias between the observed bending angle and the National Center for Atmospheric Research (NCAR) climatology model bending angle between 60 and 80 km, were used for statistical analysis. It is found that in middle and low latitudes during the daytime, the failed inverted RO occurrence and the bending angle oscillation show obvious latitude, longitude, and local time variations, which correspond well with the Es occurrence features. The F region irregularity (FI) contributes to the obvious increase of the failed inverted RO occurrence rate and the bending angle oscillation value during the nighttime over the geomagnetic equatorial regions. For high latitude regions, the Es can increase the failed inverted RO occurrence rate and the bending angle oscillation value during the nighttime. There also exists the seasonal dependency of the failed inverted RO event and the bending angle oscillation. Overall, the ionospheric irregularity effects on GNSS atmospheric RO measurement

30 exist in terms of failed RO event inversion and bending angle oscillation statistically. Awareness of these

31 effects could benefit both the data retrieval and applications of RO in the lower atmosphere.

32

33 **1. Introduction**

34 The radio occultation (RO) is a technique originally developed in the late 1960s and early 1970s for

35 planetary atmosphere exploring. With the great development of the Global Navigation Satellite System

36 (GNSS) over the past 30 years, the GNSS signal has been an effective source for exploring the Earth's

37 atmosphere. Several RO missions such as the Global Positioning System Meteorology (GPS/MET), the

38 Challenging Minisatellite Payload (CHAMP) (Wickert et al., 2001), the Scientific Application Satellite-

39 C (SAC-C), the Gravity Recovery and Climate Experiment (GRACE) (Beyerle et al., 2005), the

40 Constellation Observing System for Meteorology, Ionosphere and Climate (COSMIC) (Schreiner et al.,

41 2007), the Meteorological Operational Satellite Program (Metop) A/B, the Fengyun-3C (FY-3C) (Mao

42 et al., 2016) and et al have proven the good capability of RO for observing the Earth's ionosphere and

43 atmosphere. High-quality products of RO have been used for space weather, weather and climate

44 research (Anthes et al., 2008).

45

46 The RO technique could be divided into the ionospheric RO and the atmospheric RO. For the former one,

47 the GNSS signal propagates through the ionosphere. Dual-frequency pseudo-range and carrier phase can

48 be observed by the receiver onboard the low Earth orbit (LEO) satellite and be used to invert the electron

49 density profile. Besides, the amplitude and phase measurements can be used to calculate the ionospheric

50 scintillation index such as the S4 index. The S4 index is defined as the standard deviation of the received

51 signal power normalized to the average signal power, it can represent the occurrence of the ionospheric

52 irregularity (Yue et al., 2016). . For the latter one, the GNSS signal propagates through both the

53 ionosphere and the neutral atmosphere. The dual-frequency carrier phase can be used to calculate the

54 bending angle and then invert the atmospheric parameters. As a result, the effects on signals caused by

55 the ionosphere should be removed before deriving the atmospheric RO products.

56

57 For atmospheric RO, the GNSS signal is mainly affected by the ionosphere in two ways. Firstly, the

58 existence of dense ionospheric electron density contributes to the bending of signals. Similar to the first-

order ionospheric term calibration used in ground-based dual-frequency observations, a linear combination of the two-band signal bending at the same impact parameter is usually used to remove the ionospheric effect (Vorob'ev and Krasil'nikova, 1994). However, after the linear combination of bending angles, there still exists a residual ionospheric error (RIE). The RIE could bring ionospheric variability such as solar cycle, local time, and seasonal variations into atmospheric RO products although its amplitude is relatively low (Li et al., 2020). It means that the climate research using atmospheric RO products would be affected by the ionosphere. Some efforts have been tried for the RIE calibration (Danzer et al., 2013, 2015, 2020; Healy and Culverwell, 2015; Angling et al. 2018; Liu et al., 2018, 2020; Li et al., 2020). Danzer et al. (2013) have analyzed the bending angle bias of CHAMP and COSMIC RO data from 2001-2011 and tried to parameterize bending angle bias versus the solar cycle to make statistical corrections. Healy and Culverwell (2015) found a good correlation between the RIE and the difference of GPS L1 and L2 bending angles at the same impact parameter. They then proposed a correction method using the 'kappa' parameter under the ionospheric spherical symmetry assumption. This method was further tested by Danzer et al. (2015), Angling et al. (2018) and Danzer et al. (2020). It can reduce the systematic errors vary with solar cycle from 0.2 K to 2.0 K at altitudes between 40 km to 45 km. Liu et al. (2018) have analyzed the ionospheric structure influences on RIE in bending angles based on ray tracing simulations and further developed a "Bi-local correction approach" to calculate the RIE through an equation. This method considers both the ionospheric asymmetry effects as well as the geomagnetic effects on bending angles (Liu et al., 2020). In our previous study, we have also characterized the RIE effects statistically by both ray-tracing simulation and data analysis (Li et al., 2020). Secondly, the small-scale irregularities in the ionosphere also have an impact on the GNSS signal and finally affect the atmospheric RO products. The small-scale irregularities of which interest to this study are the sporadic E (Es) and the F region irregularity (FI). As indicated by former studies, the ionospheric irregularity will cause refraction or diffraction of the GNSS signal during its propagating through the ionosphere. The received signals could show temporal fluctuations in both amplitude and phase, which is known as the ionospheric scintillation. The impact of the small-scale irregularity on atmospheric RO can be significant but show quite different climatologically characteristics in comparison with the large-scale ionospheric effects (Li et al., 2020). Besides, it is difficult to model the ionospheric irregularity in a deterministic fashion for simulation research (Mannucci, et al., 2011). Previous studies only pointed

88 out this small scale ionospheric effect in terms of cases (Zeng and Sokolovskiy, 2010). To our knowledge,

89 there is no comprehensive study giving statistical analysis between ionospheric irregularity and

90 atmospheric RO products, which is quite important to quantify this effect and therefore benefit

91 atmospheric RO data retrieval and application. This is the main objective of this study.

92

93 In the following sections, we try to study the ionospheric irregularity effects on GNSS atmospheric RO

94 measurement statistically. Based on previous related studies, the current study will make sense as

95 following advantages: (1) the correlation between failed inverted COSMIC RO events and the

96 ionospheric irregularity are analyzed; (2) morphology of the bending angle oscillation in the atmospheric

97 RO measurement are presented in comparison with the occurrence rate of both Es and FI; (3) the seasonal

98 dependency of failed inverted RO events and the bending angle oscillation is analyzed. We will describe

99 the COSMIC observation and the statistical method in Section 2 and Section 3, respectively. Then the

100 ionospheric irregularity effects on single RO cases will be shown in Section 4. The statistical results of

101 the failed inverted RO event and the bending angle oscillation will be depicted in comparison with the

102 ionospheric irregularity occurrence rate in Section 5. Finally, the conclusions and implications will be

103 presented in Section 6.

104

105 **2. RO Data Description**

106 COSMIC, as one of the most successful RO missions, was launched on 15 April 2006. The constellation

107 with six LEO satellites has contributed millions of profiles for space weather, weather, and climate

108 research in the past 14 years. Each COSMIC satellite has four separate antennas: two high gain

109 occultation antennas received GNSS signals with a 50 Hz sampling rate to explore the neutral atmosphere

110 from the top (~130 km) to bottom or reverse. The carrier phase modulated on signals can be used for

111 excess phase calculating and atmospheric parameters retrieving. The other two antennas are precise orbit

112 determination (POD) antennas with a 1 Hz sampling rate. The received signals are used for LEO orbiting,

113 ionosphere electron density, slant total electron content (TEC), and scintillation index calculating

114 (Schreiner et al., 2007, 2011). The COSMIC data are processed by the COSMIC Data Analysis and

115 Archive Center (CDAAC) of the University Corporation for Atmospheric Research (UCAR) and

116 available on the CDAAC website (http://cdaac-www.cosmic.ucar.edu/). In this study, the COSMIC RO

observations during 2011-2013 were used for analysis. The S4 scintillation index in auxiliary data file

(scnLv1) was used for the Es and FI occurrence rates calculation. The dry atmospheric profiles file

(atmPrf) were used for the failed inverted RO occurrence rate calculation and the atmospheric bending

angle oscillation morphology analysis. The specific calculating method will be introduced in the

following section.

3. Analysis Method

To study the ionospheric irregularity effects on RO, we focus on analyzing two parameters: the failed

inverted RO event occurrence rate and the bending angle oscillation defined as the mean standard

deviation of the bias between the observed bending angle and the NCAR climatology model bending

angle during the 60-80 km altitude interval. The failed inverted RO event means those events flunked

the quality control during profiles inversion in CDAAC. They are identified by the 'bad' attribute in the

atmPrf file whose values are equal to 1. The oscillation of atmospheric RO bending angle is also provided

by the atmPrf file. The S4 index contained in the scnLv1 file is used to represent the occurrence of the

ionospheric irregularity. The occurrence rate of S4 index larger than 0.3 is set to represent the occurrence

of ionospheric irregularity. It should be noted that we identify the occurrence altitude range between

50~600 km as the contribution of both Es and FI together. We first calculated the failed inverted RO

event occurrence rate in comparison with the ionospheric irregularity occurrence rate. After that, failed

inverted RO events of COSMIC during 2011-2013 were screened out to study the Es and FI effects on

the bending angle observation. Additionally, the ionPrf file of CDAAC is used for displaying the electron

density profiles in single cases.

4. Ionospheric Irregularity Effect on Single RO Cases

To have a preliminary knowledge of the ionospheric irregularity effect on atmospheric RO, we firstly

show several typical single case examples. The results are shown in Figure 1. From top to bottom, each

row show results of a case. The three cases represent the RO event without ionospheric irregularity, the

RO event affected by the Es, and the event affected by the FI, respectively. From left to right columns,

the panels represent the inverted bending angles, the signal-to-noise ratio (SNR) of L1 C/A signal, the

related electron density profile, and the inverted dry temperature profile compared with the European

146 Centre for Medium-Range Weather Forecasts (ECMWF) results. Please note that the grey lines in the

147 rightmost panels denote the results of RO inverted temperature and the red lines represent those of

148 ECMWF. The purple lines in case 1 and case 3 are the temperature bias multiplied by 10 for convenient

149 comparison. The features of L1 C/A SNR profile and the electron density profile could identify whether

150 a RO event is affected by the ionospheric irregularity (Yue et al., 2015). As depicted in the second column,

151 the case 2 shows visible peaks in SNR fluctuation around 110 km, which correspond to the occurrence

152 altitude range of Es and could reflect the Es effects on this event. Besides, the electron density profile of

153 case 3 shows obvious scintillation between 200 km and 300 km, which implies the FI impact on signals.

154 We also use the corresponding CDAAC scnLv1 file for verification. The S4 maximum values of cases

155 1-3 are 0.03, 0.59, and 1.21, with S4 peaks around 111.69, 108.45, and 274.86 km, respectively. It can

156 be seen that the normal case shows good inversion results. The value of the ionospheric-corrected LC

157 bending angle above 40 km is much smaller than those of the L1 and L2 bending angles. It means that

158 the ionosphere dominates the bending of the RO signal in this tangent altitude interval and the linear

159 combination method works well. The bias between the observed dry temperature and the ECMWF result

160 is insignificant. However, the Es case shows bad results. Values of the inverted L2 bending angle are

161 negative, which leads to larger values of LC bending angle after the linear combination. As a result, the

162 temperature profile is failed inverted. Significant temperature bias between the observation and model

163 result can be seen from the rightmost panel. For the FI case, oscillations can be seen in the LC bending

164 angle profile in the leftmost panel as well as the temperature bias profile in the rightmost panel. The

165 bending angle oscillation values of cases 1-3 are 0.66, 16.06, and 5.74 μrad, respectively. It indicates

166 that this oscillation could also be related to the ionospheric irregularity. The geometry of atmospheric

167 RO observation determines that the ionospheric irregularity effects could propagate to a deep tangent

168 height, where far below the altitude range of irregularity occurrence (Wu, 2020). We have gone through

169 many cases and found that the failed inverted RO event and strong bending angle oscillation occurs

170 usually along with Es and FI occurrence. But not all events affected by the Es and FI are failed inverted.

171 The analysis of single cases motivates our further statistical study.

172

173 **5. Statistical Results**

174 The Es and FI have been investigated comprehensively in the past several decades (Hocke et al., 2001;

175   Straus et al., 2003; Wu, 2005; Arras et al., 2008, 2009; Carter et al., 2013; Yue et al., 2015, 2016).

176   Generally, the Es can be seen as thin layers with much higher plasma density than the normal E region

177   density occurring during the altitude range of ~ 90-120 km. The occurrence rate of Es is controlled by

178   many factors such as the tidal wind, the Earth's geomagnetic field, and metal ions (Axford, 1963; Chu et

179   al., 2014). These factors lead to the complicate variations of Es along with latitude, longitude, altitude,

180   local time, and season (Hocke et al., 2001; Wu, 2005; Arras et al., 2008, 2009). FI is the plasma

181   irregularity and inhomogeneity in the F region caused by plasma instabilities (Dungey, 1956; Fejer and

182   Kelley, 1980). The scale sizes of the density irregularity range from a few centimeters to hundreds of

183   kilometers and the irregularity can appear at all latitudes. Both Es and FI have been observed by

184   ionosonde, incoherent/coherent scatter radars, and ground-based GNSS network. Since the success of

185   GPS/MET, the GNSS RO has also been proven as an effective technique to detect the occurrence of Es

186   and FI. Hocke et al. (2001) first derived the occurrence of Es from the GPS/MET observation and

187   confirmed its seasonal variation. Wu (2005) studied the latitude, local time, altitude, and seasonal

188   dependency of Es by using CHAMP occultation data. Arras et al. (2008) further investigated the

189   occurrence of Es using multiple RO missions including CHAMP, GRACE-A, and COSMIC. Chu et al.

190   (2014) presented the morphology of Es based on COSMIC amplitude and phase fluctuations of L-band

191   signals. For FI, Straus et al. (2003) made a statistical analysis of the GPS C/A code SNR fluctuations on

192   L1 frequency based on observations onboard the PICOSat satellite. They found that the geographic and

193   local time distributions of occultation having large values of the S4 index were consistent with known

194   scintillation climatology. Brahmanandam et al. (2012) presented the three-dimensional global

195   morphology and seasonal variations of S4 index measured from COSMIC for a low solar activity year

196   2008 and found the latitude, altitude, and local time dependency of FI. Carter et al. (2013) further

197   revealed the longitudinal and seasonal variations of equatorial FI using COSMIC S4 index. Besides, Yue

198   et al. (2015, 2016) also studied the complex Es and the ionospheric irregularity related GPS RO loss of

199   lock by COSMIC S4 index.

200

201   As investigated in the single case section, the failed inverted RO event and bending angle oscillation

202   could be related to the ionospheric irregularity. So we carried out statistical research from all COSMIC

203   atmospheric events during 2011-2013. Firstly, the RO event whose 'bad' attribute in the atmPrf file equals

204   to 1 was selected as the failed inverted RO for the statistics. Then the failed inverted RO events were

205   screened out for the bending angle oscillation study. The geographical and geomagnetic distributions of

206   Es and FI are plotted separately in Figure 2. The mixed Es and FI occurrence rate, the failed inverted RO

207   event occurrence rate and the bending angle oscillation are shown in Figure 3. The grid resolutions are

208   10° ×3° for Lon×Lat and 3° ×2 h for MLat×MLT, respectively.

209

210   As depicted in Figure 3, the global geographical distribution of both Es and FI occurrence rate together

211   is depicted in the top left panel. For low and middle latitudes, two peaks of Es occurrence rate locate in

212   the East Asia region and the North Africa region in the northern hemisphere. One peak locates near the

213   South America region. The values of occurrence rate are greater than 30% in peak regions. One trough

214   can be seen around the South Africa region with an occurrence rate lower than 10%. The result

215   corresponds well with the Es characteristics derived from the GPS RO phase and SNR fluctuations (Wu,

216   2005). Besides, an occurrence enhancement can be seen around the West Africa and the Atlantic Ocean

217   region, which agrees with the previous studies base on COSMIC S4 index (Brahmanandam et al., 2012;

218   Yue et al., 2016) and indicates the contributions of FI. For high latitudes, two peaks are available during

219   120° W-150° W and 0°-60° E in the northern hemisphere and one peak can be seen around 120° E near

220   North Antarctica. In the top middle panel, we plotted the occurrence rate of failed inverted RO events

221   during 2011-2013. The rate represents the failed inverted RO event in percentage which was calculated

222   based on all observed COSMIC RO events during this time interval. Overall, the global distribution of

223   the failed inverted RO event occurrence agrees with those of the Es occurrence in the top left panel. Two

224   peaks in the northern hemisphere and one in the southern hemisphere match the locations of Es

225   occurrence peaks around ±20°. Besides, there exists an obvious increase in the failed inverted RO events

226   in high latitudes. It should be noted that the occurrence rate distribution of failed inverted RO event can't

227   match those of Es and FI completely because the inversion error is not only affected by the ionospheric

228   irregularity but also affected by other factors such as the low SNR. However, the contribution of FI on

229   the failed inverted RO event is not obvious in this panel. This might be due to the high occurrence regions

230   of FI overlaps those of Es partly. In the top right panel, we plotted the global distributions of the median

231   bending angle oscillation. The results are also in good agreement with those patterns of Es and FI

232   occurrence rate. Strong oscillations can be seen around North Africa and the East Asia regions in the

233   Northern Hemisphere and around South America in the Southern Hemisphere, with bending angle

234   oscillation values of ~1.4 μrad. The trough of bending angle oscillation can be seen around the South

235   Africa regions with values less than 1 μrad. Both the locations of peaks and troughs correspond well

236   with those of Es occurrence rate. Besides, larger oscillation values are available in the Atlantic Ocean

237   around the equator, which could be related to the high FI occurrence in these regions. Especially, both

238   the failed inverted RO and the bending angle oscillation show obvious peaks around 120° E near North

239   Antarctica. Peaks of the two parameters could be related to the high occurrence of both Es and FI in this

240   region. Peaks of Es and FI occurrence in this region have also been observed by Wu (2020) based on S4

241   index from RO data sets.

242

243   We also plotted the geomagnetic local time and latitude (MLT-MLat) distribution of the three parameters

244   in the bottom panels in Figure 3 for further comparison. In most regions of the bottom left panel, the

245   distributions are similar to those of the Es. Irregularity occurs more around geomagnetic equator regions

246   and the aurora oval regions. Around the geomagnetic equator regions during 18-24 MLT, there is an

247   occurrence enhancement caused by FI. Both Es and FI contributes to a 'three peaks' feature in the equator

248   regions after sunset. These features correspond to the previous studies observed no matter by ground-

249   based GNSS observations (Li et al., 2011) or COSMIC RO observations (Chen and Huang, 2017).

250   Similar features can be seen in the bottom middle panel. The occurrence rate of the failed inverted RO

251   event is higher around the equator regions from sunset to midnight, which can reach 20%. In high

252   latitudes, two ovals are available. Besides, the failed inverted RO event also occurs more after midnight

253   and during the noon in the Southern Hemisphere. In these regions, the FI could make contributions. For

254   bending angle oscillation in the bottom right panel, three peaks of the mean oscillation value exist along

255   the geomagnetic latitude, which denotes the contribution of Es and FI during the nighttime. The value of

256   bending angle oscillation tends to be small within $\pm 60°$ during 2~10 MLT. For high latitudes, the

257   bending angle shows strong oscillation even though the occurrence rate of Es and FI is lower than those

258   of peak regions in middle and low latitudes.

259

260   For a better display of the high-latitude results, we plotted the irregularity and failed inverted RO

261   occurrence rates as well as the bending angle oscillation variation with MLT-MLat in northern and

262 southern polar regions in Figure 4. As depicted in the left two panels, the ionospheric irregularity mainly

263 occurs during 18-24 MLT, with occurrence peaks existing in aurora regions around midnight and moving

264 toward the polar cap regions when approaching the sunset time. Values of the irregularity occurrence rate

265 are around 10-20% during the nighttime and can reach 30% for peak regions. The middle two panels

266 show the occurrence rate of failed inverted RO events. It is depicted that the peaks are located in aurora

267 regions and extent to the polar cap regions from sunset time to midnight. The increase in the occurrence

268 rate around these regions might be affected by the high occurrence rate of Es. The failed inverted RO

269 occurrence rates are also higher during the daytime in both hemispheres although the irregularity

270 occurrence rates are lower than 10% during this period. The right panels show the bending angle

271 oscillation results. Its value is larger in aurora regions around midnight, which can reach 2.1 μrad. For

272 those values in the South Hemisphere, strong bending angle oscillation can be seen in the polar cap

273 regions no matter during the daytime or nighttime. Besides, the peak regions locate mainly between

274 80° S-90° S instead of the 70° S-80° S as the irregularity occurrence peak shown in the bottom middle

275 panel.

276

277 We also use the scatter plot to study correlations between the ionospheric irregularity and the two

278 parameters. The results were plotted in Figure 5. Considering patterns of the failed inverted RO

279 occurrence rate and the bending angle oscillation could not agree very well with those of the irregularity

280 in high latitude regions, we mainly pay attention to the results in low and middle latitudes (60° S-60° N).

281 Correlations during the daytime (6~18 MLT) and the nighttime (0~6, 18~24 MLT) were displayed

282 respectively. Overall, the correlations between the ionospheric irregularity and the two parameters are

283 significant although they are not strictly liner especially for the bending angle oscillation during the

284 daytime. The scatters in the panels are probably due to that the bending angle oscillation is not only

285 affected by the Es and FI but also related to other factors. Meanwhile, the observation and inversion noise

286 could also make contributions.

287

288 In Figures 3-5, we mainly concern about the yearly average pattern. As stated above, the seasonal

289 variation of irregularity has been confirmed by previous studies (Arras et al., 2008; Chen and Huang,

290 2017). So the seasonal dependency of the failed inverted RO event and the bending angle oscillation

291   could also exist. For further investigating, the occurrence rate variation with Lon-Lat and MLT-MLat

292   were depicted in Figure 6 and Figure 7, respectively. Equinox (March, April, September, and October),

293   Northern Summer (May, June, July, and August), and Northern Winter (January, February, November,

294   and December) are considered here. Generally, in Figure 6, the distributions of the failed inverted RO

295   event occurrence are in good agreement with those of the irregularity. Both parameters are larger within

296   ±30° in Equinox and larger in summer than in winter. For Northern Summer, the occurrence peaks are

297   near the North Africa area and the East Asia area. For Northern Winter, the peaks are available in the

298   Pacific Ocean regions nearby South America. Similar to the average pattern in Figure 3, the failed

299   inverted RO occurrence rate is high in polar regions even though the Es and FI occurrence is not obvious

300   in comparison with those of peak regions in low latitudes. The MLT-MLat distributions of the irregularity

301   and the failed inverted RO in Figure 7 also show similar seasonal variations. But for the southern polar

302   region in Equinox and the northern polar region in Northern Winter, the failed inverted RO occurs

303   significantly on condition that the occurrences of Es and FI are not obvious. For the bending angle results

304   in both bottom panels in Figures 6 and 7, it is apparent that the bending angle oscillation value also

305   follows a similar seasonal variation with the ionospheric irregularity occurrence, which is larger in

306   summer than in winter with the equinox as the transitory season. It is noticeable that for the geographic

307   distribution, larger values exist around Northern Antarctica in all seasons. For the geomagnetic

308   distributions, the three peaks along geomagnetic latitudes are available in all seasons.

309

6.   Conclusions and Implications

311   In this paper, we focus on the ionospheric irregularity effects on GNSS atmospheric RO. The failed

312   inverted RO events and the bending angle oscillation are the two main parameters we concerned about.

313   The COSMIC S4 index provided by CDAAC during 2011-2013 is used to characterize the ionospheric

314   irregularity occurrence rate such as the Es and the F region irregularity. The 'bad' attribute in the atmPrf

315   file is used to identify the failed inverted RO events on condition that its value equals to 1. The mean

316   bending angle oscillation also from the atmPrf file is used to reflect the degree of bending angle

317   oscillation. Results from single cases are analyzed firstly. Then the distribution patterns and seasonal

318   variations of the ionospheric irregularity occurrence rate, failed inverted RO event occurrence rate, and

the bending angle oscillation are presented for the correlation study. The main conclusions and implications of the paper are summarized in the following:

(1) The ionospheric irregularity such as the Es and the F region irregularity could affect the GNSS atmospheric RO in terms of causing failed inverted RO events and the bending angle oscillation in both cases and statistically.

(2) In middle and low latitudes, during the daytime, both the failed inverted RO event and the bending angle oscillation are mainly affected by the Es. During the nighttime, the F region irregularity contributes to the obvious increases of the failed inverted RO occurrence rate and the bending angle oscillation around the geomagnetic equatorial regions.

(3) In the polar regions, the Es mainly affect the two parameters in the aurora regions from sunset to midnight. But the correlations between the ionospheric irregularity and the two parameters are not as obvious as those in middle and low latitudes.

(4) Seasonal dependency of the failed inverted RO occurrence and the bending angle oscillation exists, which also accord well with the seasonal variation of the Es and the F region irregularity.

(5) The occurrence rate of the failed inverted RO can reach 15% in low latitudes and even 20% in peak regions. It means that hundreds of COSMIC RO events per day will be ruled out during quality control. The bending angle oscillation between 60 and 80 km also varies from ~0.6 μrad in trough regions to ~2.5 μrad in peak regions. Although 60~80 km is not the main altitude range of RO data, the small-scale effects in atmospheric RO exist in all altitudes and could affect the atmospheric research related to RO products. Awareness of the ionospheric irregularity effect on RO could be beneficial to improve the data retrieval, quality control of GNSS atmospheric RO data processing and data assimilation application in numerical weather prediction (Cardinali and Healy, 2014).

Overall, the ionospheric irregularity effects on GNSS atmospheric RO measurement exist in terms of failed RO event inversion and bending angle oscillation statistically. It makes the calibration of ionospheric irregularity effects on RO more challenging and urgent. A suitable filter may be helpful in reducing the ionospheric irregularity effects on bending angles and including ruled-out events in the processing. The potential method needs to be more investigated and we hope to study it in our further work. Besides, the causing of failed inverted RO events in high latitudes is also needed to be studied.

347 **7.   Acknowledgement**

348 This work was supported by the B-type Strategic Priority Program of the Chinese Academy of Sciences

349 (Grant No. XDB41000000), the Open Research Project of Large Research Infrastructures - "Study on

350 the interaction between low/mid-latitude atmosphere and ionosphere based on the Chinese Meridian

351 Project", the National Natural Science Foundation of China (41427901), and the Key Research Program

352 of the IGGCAS with Grant No. IGGCAS-201904. The University Corporation for Atmospheric Research

353 (UCAR) COSMIC Data Analysis and Archive Center (CDAAC) is appreciated for processing and

354 sharing the COSMIC radio occultation data to the community over years. All the data used in the study

355 could be downloaded from the CDAAC website (http://cdaac-www.cosmic.ucar.edu/).

356

357 **8.   References**

358 Axford, W. I.: The formation and vertical movement of dense ionized layers in the ionosphere due to

359 neutral wind shears, Journal of Geophysical Research, 68, 769–779, doi:10.1029/JZ068i003p00769,

360 1963.

361 Anthes, R. A., Bernhardt, P. A., Chen, Y., Cucurull, L., Dymond, K. F., Ector, D., Healy, S. B., Ho, S. P.,

362 Hunt, D. C., Kuo, Y. H., Liu, H., Manning, K., McCormick, C., Meehan, T. K., Randel, W. J., Rocken,

363 C., Schreiner, W. S., Sokolovskiy, S. V., Syndergaard, S., Thompson, D. C., Trenberth, K. E., Wee, T. K.,

364 Yen, N. L., and Zeng, Z.: The COSMIC/FORMOSAT-3 mission: Early results, Bulletin of the American

365 Meteorological Society, 89, 313–333, doi.org/10.1175/BAMS-89-3-313, 2008.

366 Angling, M. J., Elvidge, S., and Healy, S. B.: Improved model for correcting the ionospheric impact on

367 bending angle in radio occultation measurements, Atmospheric Measurement Techniques, 11, 2213-2224,

368 doi.org/10.5194/amt-11-2213-2018, 2018.

369 Arras, C., Wickert, J., Beyerle, G., Heise, S., Schmidt, T., and Jacobi, C.: A global climatology of

370 ionospheric irregularities derived from GPS radio occultation, Geophysical Research Letters, 35,

371 doi:10.1029/2008gl034158, 2008.

372 Arras, C., Jacobi, C., and Wickert, J.: Semidiurnal tidal signature in sporadic E occurrence rates derived

373 from GPS radio occultation measurements at higher midlatitudes, Ann Geophys, 27, 2555–2563, 2009.

374   Beyerle, G., Schmidt, T., Michalak, G., Heise, S., Wickert, J., and Reigber, C.: GPS radio occultation

375   with GRACE: Atmospheric profiling utilizing the zero difference technique, Geophysical Research

376   Letters, doi.org/10.1029/2005gl023109, 2005.

377   Brahmanandam, P. S., Uma, G., Liu, J. Y., Chu, Y. H., Latha Devi, N.S.M.P., and Kakinami, Y.: Global

378   S4 index variations observed using FORMOSAT-3/COSMIC GPS RO technique during a solar minimum

379   year, Journal of Geophysical Research: Space Physics, 117, doi:10.1029/2012ja017966, 2012.

380   Cardinali, C. and Healy, S.: Impact of GPS radio occultation measurements in the ECMWF system using

381   adjoint-based diagnostics, Quarterly Journal of the Royal Meteorological Society, 140, 2315-2320,

382   doi:10.1002/qj.2300, 2014.

383   Carter, B.A., Zhang, K., Norman, R., Kumar, V. V., and Kumar, S.: On the occurrence of equatorial F-

384   region irregularities during solar minimum using radio occultation measurements, Journal of

385   Geophysical Research: Space Physics, 118, 892-904, doi:10.1002/jgra.50089, 2013.

386   Chu, Y. H., Wang, C. Y., Wu, K. H., Chen, K. T., Tzeng, K. J., Su, C. L., Feng, W., and Plane, J. M. C.:

387   Morphology of sporadic E layer retrieved from COSMIC GPS radio occultation measurements: Wind

388   shear theory examination, Journal of Geophysical Research: Space Physics, 119, 2117-2136,

389   doi:10.1002/2013ja019437, 2014.

390   Chen, S. and Huang, Z.: Ionospheric F-layer global scintillation index variation using COSMIC during

391   the period of 2007–2013, GPS Solutions, 21, 1049-1058, doi:10.1007/s10291-016-0593-2, 2017.

392   Dungey, J. W.: Convective diffusion in the equatorial F region, Journal of Atmospheric and Terrestrial

393   Physics, 9, 304-310, doi.org/10.1016/0021-9169(56)90148-9, 1956.

394   Danzer, J., Scherllin-Pirscher, B., and Foelsche, U.: Systematic residual ionospheric errors in radio

395   occultation data and a potential way to minimize them, Atmospheric Measurement Techniques, 6, 2169-

396   2179, doi.org/10.5194/amt-6-2169-2013, 2013.

397   Danzer, J., Healy, S. B., and Culverwell, I. D.: A simulation study with a new residual ionospheric error

398   model, for GPS radio occultation climatologies, Atmospheric Measurement Techniques, 8, 3395-3404,

399   doi.org/10.5194/amt-8-3395-2015, 2015.

400   Danzer, J., Schwaerz, M., Kirchengast, G., and Healy, S. B.: Sensitivity analysis and impact of the kappa-

401 correction of residual ionospheric biases on radio occultation climatologies, Earth and Space Science, 7,

402 e2019EA000942, doi.org/10.1029/2019EA000942, 2020.

403 Fejer, B. G. and Kelley, M. C.: Ionospheric irregularities. Reviews of Geophysics, 18, 401–454,

404 doi:10.1029/RG018i002p00401, 1980.

405 Hocke, K., Igarashi, K., Nakamura, M., Wilkinson, P., Wu, J., Pavelyev, A., and Wickert, J.: Global

406 sounding of sporadic E layers by the GPS/MET radio occultation experiment, Journal of Atmospheric

407 and Solar-Terrestrial Physics, 63, 1973–1980, 2001.

408 Healy, S. B., Culverwell, I. D.: A modification to the standard ionospheric correction method used in

409 GPS radio occultation, Atmospheric Measurement Techniques, 8, 3385-3393, doi.org/10.5194/amt-8-

410 3385-2015, 2015.

411 Li, G., Ning, B., Abdu, M. A., Yue, X., Liu, L., Wan, W., and Hu, L.: On the occurrence of postmidnight

412 equatorial Fregion irregularities during the June solstice, Journal of Geophysical Research: Space

413 Physics, 116, doi:10.1029/2010ja016056, 2011.

414 Liu, C., Kirchengast, G., Sun, Y., Zhang, K., Norman, R., Schwaerz, M., Bai, W., Du, Q., and Li, Y.:

415 Analysis of ionospheric structure influences on residual ionospheric errors in GNSS radio occultation

416 bending angles based on ray tracing simulations, Atmospheric Measurement Techniques, 11, 2427-2440,

417 doi.org/10.5194/amt-11-2427-2018, 2018.

418 Liu, C., Kirchengast, G., Syndergaard, S., Schwaerz, M., Danzer, J., and Sun, Y.: New Higher-Order

419 Correction of GNSS RO Bending Angles Accounting for Ionospheric Asymmetry: Evaluation of

420 Performance and Added Value, Remote Sensing, 12, doi.org/10.3390/rs12213637, 2020.

421 Li, M., Yue, X., Wan, W., and Schreiner, W. S.: Characterizing Ionospheric Effect on GNSS Radio

422 Occultation Atmospheric Bending Angle, Journal of Geophysical Research: Space Physics, 125,

423 doi.org/10.1029/2019JA027471, 2020.

424 Mannucci, A. J., Ao, C. O., Pi, X., and Iijima, B. A.: The impact of large scale ionospheric structure on

425 radio occultation retrievals, Atmospheric Measurement Techniques, 4, 2837-2850, doi.org/10.5194/amt-

426 4-2837-2011, 2011.

427 Mao, T., Sun, L., Yang, G., Yue, X., Yu, T., Huang, C., Zeng, Z., Wang, Y., and Wang, J.: First Ionospheric

Radio-Occultation Measurements From GNSS Occultation Sounder on the Chinese Feng-Yun 3C Satellite, IEEE Transactions on Geoscience and Remote Sensing, 54, doi.org/1-10. 10.1109/TGRS.2016.2546978, 2016.

Straus, P. R., Anderson, P. C., and Danaher, J. E.: GPS occultation sensor observations of ionospheric scintillation, Geophysical Research Letters, 30, doi:10.1029/2002gl016503, 2003.

Schreiner, W., Rocken, C., Sokolovskiy, S., Syndergaard, S., and Hunt, D.: Estimates of the precision of GPS radio occultations from the COSMIC/FORMOSAT-3 mission, Geophysical Research Letters, 34, doi:10.1029/2006gl027557, 2007.

Schreiner, W., Sokolovskiy, S., Hunt, D., Rocken, C., and Kuo, Y. H.: Analysis of GPS radio occultation data from the FORMOSAT-3/COSMIC and Metop/GRAS missions at CDAAC, Atmospheric Measurement Techniques, 4, 2255-2272, doi:10.5194/amt-4-2255-2011, 2011.

Vorob'ev, V. V. and Krasil'nikova, T. G.: Estimation of the accuracy of the atmospheric refractive index recovery from Doppler shift measurements at frequencies used in the NAVSTAR system, USSR, Atmospheric and Oceanic Physics, English Translation, 29, 602-609, 1994.

Wickert, J., Marquardt, C., Beyerle, G., Reigber, C., and König, R.: Atmosphere sounding by GPS radio occultation: First results from CHAMP, Geophysical Research Letters, 28, 3263-3266. doi.org/10.1029/2001gl013117, 2001.

Wu, D. L.: Sporadic E morphology from GPS-CHAMP radio occultation, Journal of Geophysical Research, doi:10.1029/2004ja010701, 2005.

Wu, D. L.: Ionospheric S4 Scintillations from GNSS Radio Occultation (RO) at Slant Path, Remote Sensing, 12, doi:10.3390/rs12152373, 2020.

Yue, X., Schreiner, W. S., Zeng, Z., Kuo, Y. H., and Xue, X.: Case study on complex sporadic E layers observed by GPS radio occultations, Atmospheric Measurement Techniques, 8, 225-236, doi:10.5194/amt-8-225-2015, 2015.

Yue, X., Schreiner, W. S., Pedatella, N. M., and Kuo, Y. H.: Characterizing GPS radio occultation loss of lock due to ionospheric weather, Space Weather, 14, 285-299, doi:10.1002/2015sw001340, 2016.

454   Zeng, Z. and Sokolovskiy, S.: Effect of sporadic E clouds on GPS radio occultation signals, Geophysical

455   Research Letters, 37, doi:10.1029/2010gl044561, 2010.

456
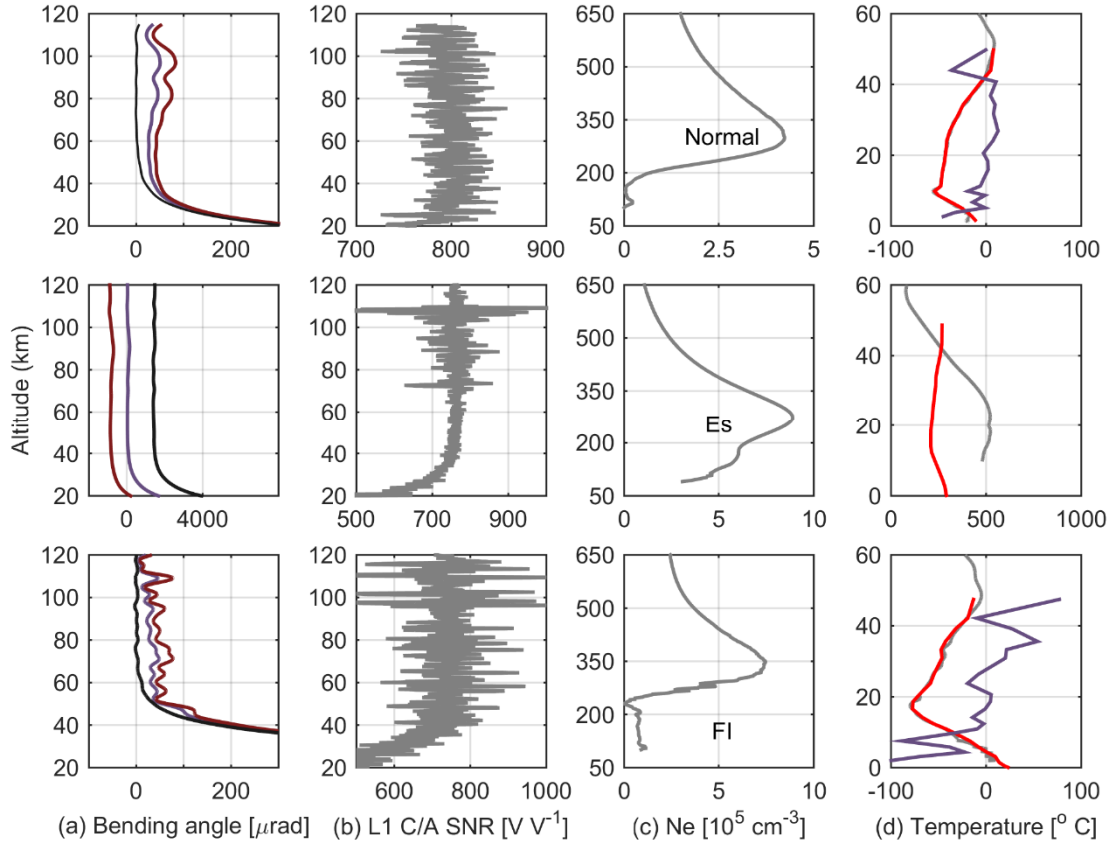
Figure 1. Example of three cases occurred in 2013 made by COSMIC. Panels from top to bottom

457

are normal example without the ionospheric irregularity occurrence, the Es example, and the F

458

region irregularity example. Panels from left to right are the inverted L1 (purple line), L2 (brown

459

line), and LC (black line) bending angles; the L1 C/A SNR, the electron density profile at the RO

460

tangent points; the inverted dry temperature (grey line) versus the ECMWF results (red line) as

461

well as their bias multiplied by 10 (purple line). Please note that the Y-axis of all panels represents

462

the altitude with kilometer (km) as the unit.

463
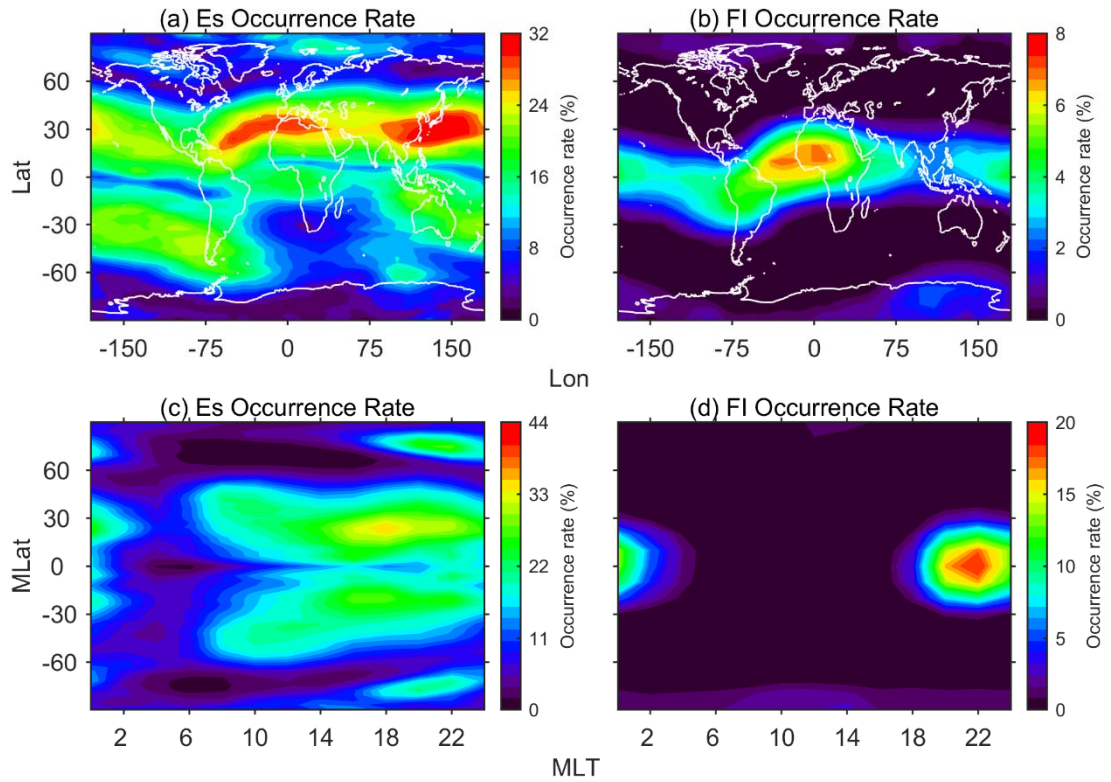
464
465   **Figure 2. Global geographical (top panels) and geomagnetic distributions (bottom panels) of the**
466   **Es (left panels) and F layer irregulary occurrence rate (right panels), during 2011-2013.**

467

468
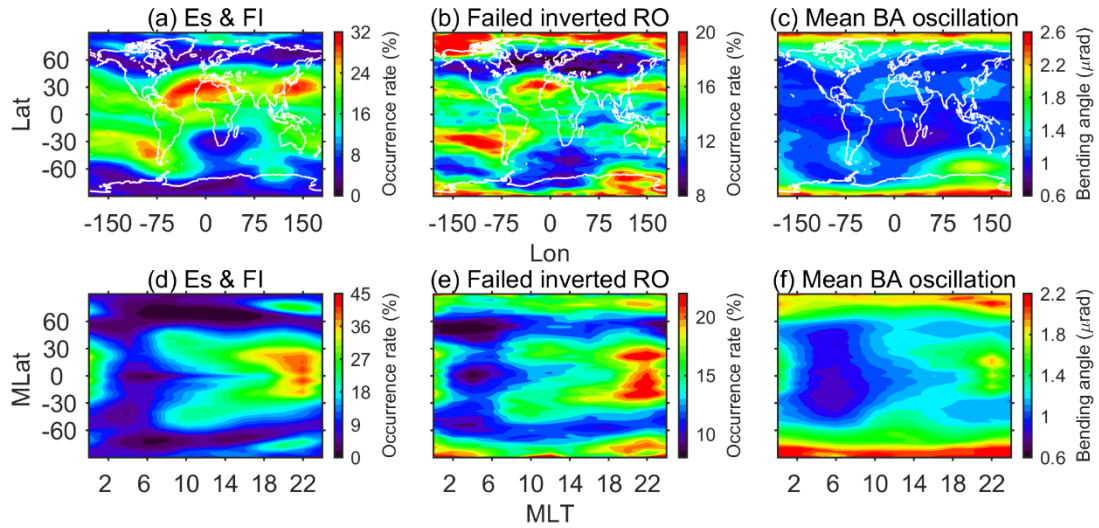
469 **Figure 3. Global geographical (top panels) and geomagnetic distributions (bottom panels) of the**

470 **Es and F layer irregularity occurrence rate (left panels), the failed inverted RO event occurrence**

471 **rate (middle panels), and the mean bending angle oscillation (right panels) during 2011-2013.**

472
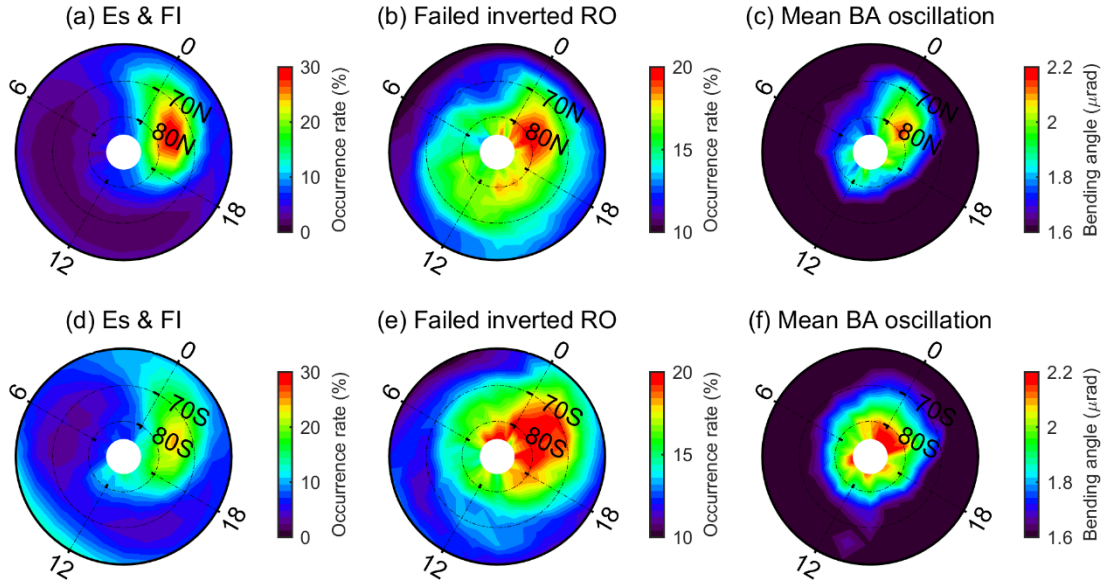
Figure 4. MLT-MLat variation of the Es and F layer irregularity occurrence rate (left panels), the

failed inverted RO occurrence rate (middle panels), and the mean bending angle oscillation (right

panels) in polar regions. Please note that the top panels represent the results in northern polar

regions while the bottom panels denote the southern polar regions.

477
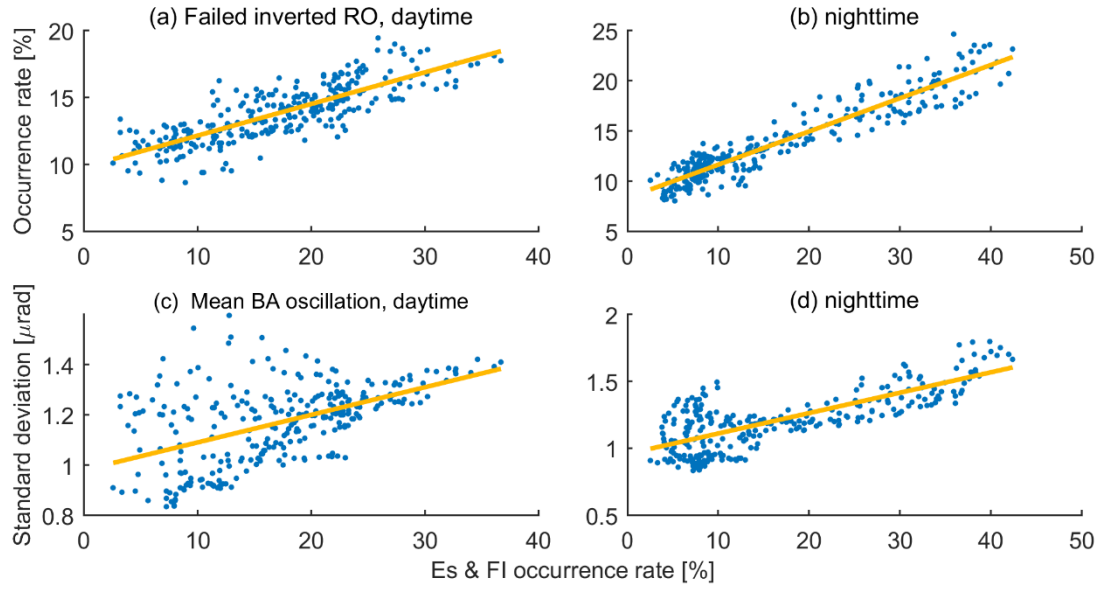
Figure 5. Correlations between the ionospheric irregularity and the two parameters in middle and low latitudes (60° S-60° N) during the daytime (6~18 MLT, left panels) and nighttime (0~6 & 18~24 MLT, right panels) of 2011-2013. The yellow line is the corresponding linear least square fitting results.

482
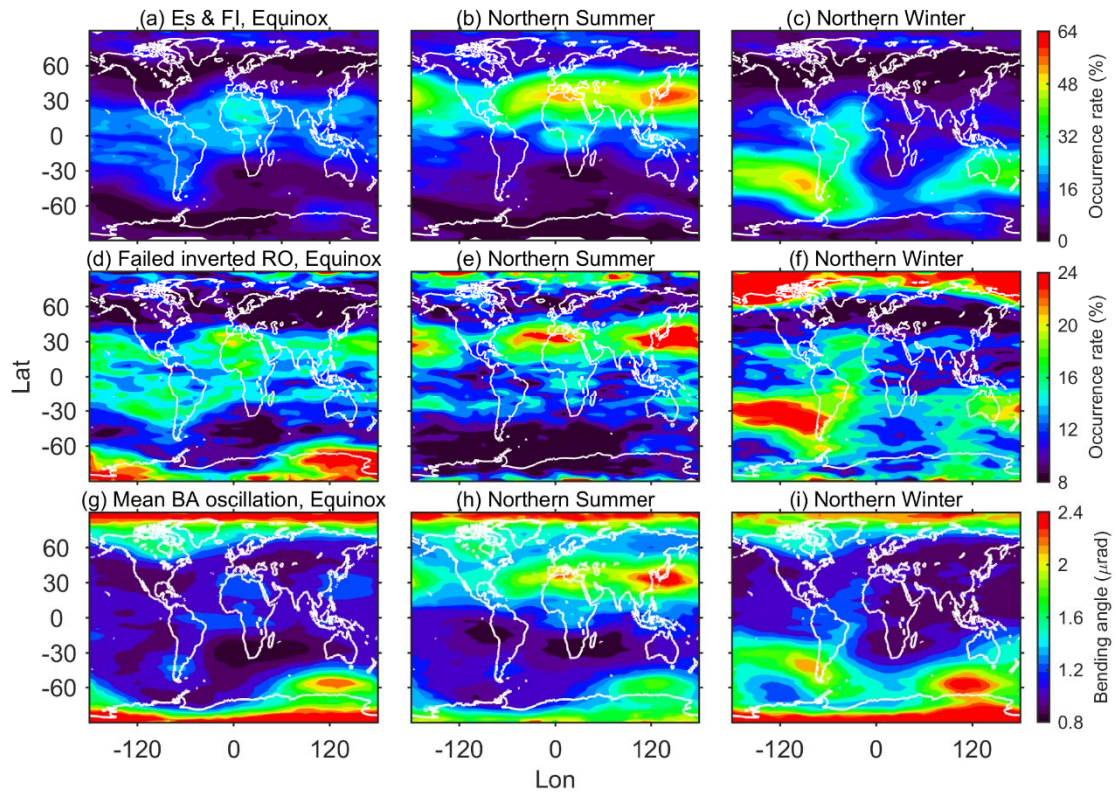
483 **Figure 6. Global geographical distribution of the Es and F layer irregularity occurrence rate (top**

484 **panels), the failed inverted RO occurrence rate (middle panels), and the mean bending angle**

485 **oscillation (bottom panels) for Equinox (left panels), Northern Summer (middle panels), and**

486 **Northern Winter (right panels).**

487
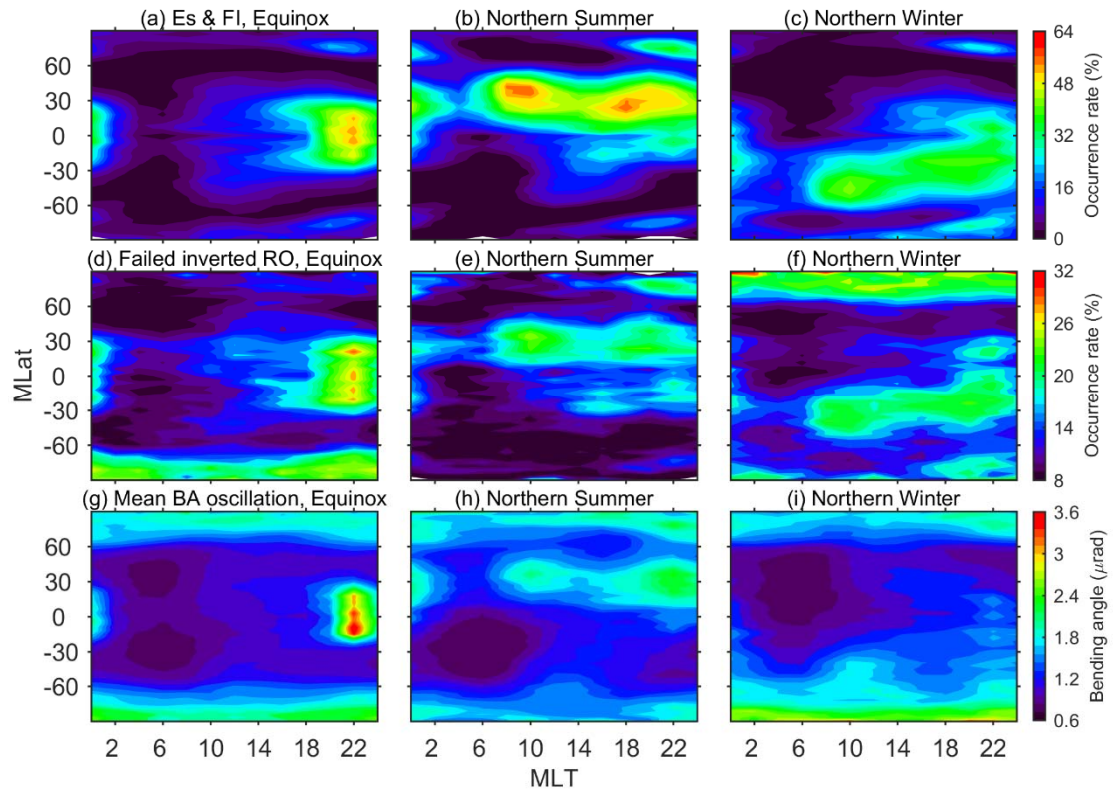
488 **Figure 7 The same as Figure 6, but for geomagnetic local time (MLT) and geomagnetic latitude**

489 **(MLat) variation.**